

## Review Article

# Manufacturing of $\beta$ -type NbXTi (X=50 at%)/SWCNTs Matrix Nanocomposites by FAST-SPS: For Metallic Orthopedic Components and Superconductor Magnets in ITER

Badis Bendjemil<sup>1,3,4</sup>, Khaoula Saffi<sup>2\*</sup>, Ilyas Kouahla<sup>2</sup>, Jacques Guillome Noudem<sup>4</sup>, Mohamed Mouyane<sup>3</sup>, Jérôme Bernard<sup>3</sup> and David Houivet<sup>3</sup>

<sup>1</sup>DGM/FST/UG-Université 08 Mai 1945 Guelma, Avenue 19 Mai 1956, CS 401, 24000 Guelma, Algeria

<sup>2</sup>LMS Laboratory, Université 8 Mai 1945 Guelma, Avenue 19 Mai 1956, CS 401, 24000 Guelma, Algeria

<sup>3</sup>LUSAC, EA 4253, 60 rue Max Pol Fouchet, CS 20082, Université de Caen Basse-Normandie (UCBN), 50130 Cherbourg-Octeville, France

<sup>4</sup>ENSICAEN, 6, Boulevard Maréchal Juin, CS 45053 14050 Caen Cedex 04, France

\*Corresponding author: Khaoula Saffi, LMS Laboratory, Université 8 Mai 1945 Guelma, avenue 19 Mai 1956, CS 401, 24000 Guelma, Algeria

Received: October 07, 2022; Accepted: October 14, 2022; Published: October 21, 2022

## Abstract

The synthesis of  $\beta$ -type phase Nb<sub>x</sub>Ti (x=50 at%)/SWCNTs intermetallic matrix nanocomposite by mechanical alloying to ensure the effective distribution of single walled carbon nanotubes (SWCNTs) within the matrix. It has been stated by several researchers that during ball-milling of Nb<sub>x</sub>Ti (x=50 at%) powder mixtures, Nb-Ti intermetallic compound formation occurs either gradually along milling time, or suddenly through a mechanically self-propagating reaction (MSPR), which occurs after a ignition time of MA. For this purpose, 0.4 and 0.8 wt% of SWNTs were added to the powder mixture after the completion of reaction between Nb and Ti. The resultant powders Nb<sub>50</sub>Ti intermetallic compound and with addition of powder of SWCNTs and then also ball-milled. Bulk samples were compacted and then sintered by field activated sintering technic spark plasma sintering method (FAST-SPS) at lower temperature in the range (1273 to 1473 K) with short time that retained the integrity of SWNTs in the intermetallic matrix. Structural and characteristics evolutions of the nanocomposites were investigated by X-ray diffractometry (XRD). Field emission scanning electron microscopy (FESEM) micrographs showed that the offered MA approach caused the SWNTs to uniformly embed in the in situ synthesized NbTi intermetallic matrix. Meanwhile better distribution of SWCNTs resulted in higher density of FAST-SPS-FCT bulk nanocomposite as well as higher hardness up to 2.75 GPa compared to 2.4 of Nb<sub>50</sub>Ti intermetallic alloy obtained from the after MA time. The total porosity, compressive strength, and compressive elastic modulus of the FAST-SPS-FCT manufactured material were determined as 7%, 600 MPa, and 120 MPa, respectively. The alloy's and its intermetallic nanocomposite have Young's elastic modulus is comparable to that of healthy cancellous bone which makes it applicable in the biomedical field. The in vitro biocompatibility will be performed in the near future. The comparable results for the FAST-SPS-FCT nanocomposites were 3%, 650 MPa, and 130 MPa. The alloy's elastic modulus is comparable to that of healthy cancellous bone. This difference in mechanical properties results from different porosity and phase composition of the bot  $\beta$ -phase Nb<sub>x</sub>Ti (x=50 at%) and Nb<sub>x</sub>Ti (x=50 at%)/SWCNTs intermetallic matrix nanocomposite.

More other nanotechnologies applications of the nanocomposite will be focused in the study of the superconducting type I for the ITER Poloidal Field Coils by measuring of J<sub>c</sub> (T, B) characteristics.

**Keywords:**  $\beta$ -type phase Nb<sub>x</sub>Ti (x=50 at%), SWCNTs, FAST-SPS-FCT, Microhardness, Fracture toughness, compressive strength, Compressive elastic modulus, Porosity architecture, Cancellous bone, ITER Poloidal Field Coils

## Introduction

Titanium and porous Ti and its alloys are widely used as load-bearing implant materials for hard tissue support and replacement because of good mechanical properties, excellent biocompatibility, and high corrosion resistance. One of the short comings of commonly-used Ti-based alloys is high stiffness, expressed as high elastic modulus (E) (typically, >100 GPa). In implant applications, a large stiffness mismatch between the implant material and the contiguous bone can lead to stress shielding, which retards the mechanical stimulation of the bone healing process. Thus, for a given

Ti-based alloy, it is desirable to reduce its E to that of healthy bone (4–30 GPa) while maintaining its high strength and good plasticity [1-8]. Two approaches have been taken to achieve this goal. One is the production of metastable  $\beta$  type phase wrought niobium-titanium (Nb-Ti) alloys (for example, Nb<sub>50</sub>Ti), but the reported minimum value of E (60–62 GPa) is too high [9,10].

Alternatively, porous Nb-Ti alloys, having a microstructure similar to that of cancellous bone, have been produced. Nb-Ti Intermetallic compound has been recognized as one of high temperature structural materials due to excellent physical, superconductivity and mechanical

properties such as low density (5.7 g/cm<sup>3</sup>), high melting point (2173°K) and excellent oxidation resistance, as well as good thermal conductivity. NbTi compound is also known for its good ductility and fracture toughness at room temperature. Several methods such as grain refinement, second-phase strengthening, mechanical alloying, selective laser melting, field assisted spark plasma sintering and hot pressing, have been offered to overcome this limitation. High energy ball mills have been used for mechanical alloying (MA) as a production method to synthesize and modify intermetallic compounds like Nb-Ti. It has been stated by several researchers that during ball-milling of Nb and Ti powder mixtures, Nb-Ti intermetallic compound formation occurs either gradually along milling time, or suddenly through a mechanically self-propagating reaction (MSR), which occurs after a certain time of ball-milling called ignition time. In the last decade ball-milling has been widely used for the fabrication of intermetallic matrix composites containing ceramic or metalloid particles. In recent years carbon nanostructures such as carbon nanotubes (CNTs), fullerene and graphene have been the focus of significant research. Carbon nanotubes (CNTs) with exceptional mechanical and physical properties offer promising potential as a reinforcing material to enhance the mechanical, thermal and electrical properties of nanocomposites. It is obvious that a successful dispersion of CNTs in the matrix is needed before any sort of significant benefits in the nanocomposite is realized. In fact, adequate dispersion of the CNTs in the matrix is still challenging. It has been concluded from several researches that MA can be considered as an effective process to achieve homogenous distribution of CNTs in metallic and intermetallic matrix. It is known that CNTs are entangled between re-welded ductile particles during milling and after appropriate time are embedded within metal and intermetallic matrix. Milling of CNTs with brittle powders like ceramics and intermetallic compounds has been reported to result in the distribution of CNTs on the surface of particles that can affect the compressibility and sinter ability of powder particles [11-29]. There are a fair number of literature reports on production and characterization of porous Nb-Ti alloy. Lin et al. [30] used powder, produced using ball-milled powder and a powder metallurgical method to fabricate Nb<sub>35</sub>Ti porous samples. The samples were produced by sintering with ammonium bicarbonate particles as space-holder. Yang et al. [31] used powder produced by high energy vibration ball milling and gel casting to fabricate Nb<sub>25</sub>Ti samples. A. Helth et al. [32,33] used commercial titanium and niobium powders and PM to fabricate Nb<sub>40</sub>Ti. Zhuravleva et al. [34,35] used ball-milled Nb<sub>40</sub>Ti powder and a space-holder method to fabricate porous samples. One of the methods that has recently been introduced for the production of porous alloys is selective laser melting (SLM). The process involves direct melting of a powder and creation of net-shaped bodies through a “layer by layer” approach. Each layer is melted by a scanning laser and is mounted on a previously molten layer. The high temperature, steep temperature gradient, and fast cooling rates involved in SLM allow stabilization of metastable phases in an alloy [36].

To the best of our knowledge there are neither studies involving the use of SLM to fabricate porous Nb-Ti alloys nor studies involving comparison of properties of a Nb-Ti alloy fabricated using different techniques but with the powder produced using the same method.

$\beta$ -type structure Nb<sub>50</sub>Ti are developed for biomedical applications because of their expected high biocompatibility and low elastic modulus in compare with conventional titanium alloys. Low elastic modulus is important with respect to biomechanical compatibility. When using an implant with high elastic modulus it overtakes a considerable part of body loading. Then the bone is shielded from necessary stressing required to maintain its strength, density and healthy structure. This effect (usually termed as “stress shielding”) may cause bone loss, implant loosening and premature failure of the implant. The addition of elements like V, which has one of the highest cytotoxicity, and Al, that is suspected from causing neurological problems (Alzheimer disease). The designing of a novel biofunctional-structure hydroxyapatite composite with enhanced mechanical properties, high bioactivity and porous low modulus Ti<sub>40</sub>Nb compacts with electrodeposited hydroxyapatite coating for biomedical applications have been studied by A. Helth et al., R. Schmidt et al. [37-39] and K. Zhuravleva et al. [40]. The addition of Zr, Si, Pd, Fe, Sn, Ta and Indium [41-44] to Beta-type Nb-Ti forming biocompatible glass, apatite formation and bulk metallic composites for novel biocompatible materials with superior mechanical strength and elastic recovery were studied intensively. The designing biocompatible Ti-based metallic glasses for implant applications were also studied and applied. Finally, Ab-initio and experimental study of phase stability of Nb-Ti alloys [45,46].

Theoretical and experimental study concerning the crystallographic structure and electronic properties of Nb<sub>x</sub>Ti (x < 50 at%) alloys is presented, aiming to enlighten the electronic origins of the  $\beta$ -phase stability which is of high interest for the development of novel  $\beta$  stabilized Ti-based alloys for biomedical applications. These data could enlighten the electronic origin of the Nb-Ti phase stability, thus, may contribute to the design of  $\beta$  stabilized low moduli Ti-based alloys suitable for load-bearing biomedical applications.

Nb-Ti is used in the TETRA tokamak systems code is used to compare designs for the International Thermonuclear Experimental Reactor (ITER) that uses Nb-Ti superconductor magnets. Its critical temperature is about 10 kelvins. The minimum-cost devices occur for peak fields at the toroidal field coil of about 11.5-13 T, depending on the physics requirements. Sensitivities to the allowable stress level indicate strong cost increases when the stress is reduced from the nominal 600 MPa level and weaker cost benefits when the stress is allowed to reach higher levels. Nb-Ti alloys have a maximal critical magnetic field of about 15 teslas, and are thus are suitable for fabricating super magnets capable of generating magnetic fields up to about 10 teslas. For higher magnetic fields, higher-performance but difficult to fabricate and thus more expensive superconductors such as niobium-tin are commonly employed. The substitution and using of the nanocomposite produced by FAST-SPS with higher density improved the superconducting properties J<sub>c</sub> (T<sub>c</sub>, B) and working with low cost. In the present study a route was proposed to synthesize Nb<sub>x</sub>Ti (x=50 at%)/0.4 to 0.8 SWCNTs by ball-milling of elemental powders 20 h to achieve effective accommodation of SWCNTs within the Nb-Ti intermetallic matrix during in situ formation of intermetallic compound. The milling time with SWCNTs was limited to 10 h to reduce the damage of single walled carbon nanotubes. 4 to 0.8 wt% SWCNTs. In the present approach SWCNTs were added to

the powder mixture after the completion of reaction between Nb and Ti. Therefore, SWCNTs could entangle between re-welding ductile powder particles before the complete evolution of particles to fully brittle intermetallic compound. The structural evolution during ball-milling was investigated. In order to obtain fully dense intermetallic nanocomposites, and minimize the decomposition of SWCNTs during sintering, FAST-SPS was employed after ball-milling in the present study. FAST-SPS, in which much lower sintering temperatures and shorter times are applicable, is an effective sintering technique for obtaining fully dense nanocrystalline composites and fine grain structure. Microstructure of powders and FAST-SPS samples was investigated, micro hardness and fracture toughness of bulk samples were evaluated. In addition, compressive strength and compressive elastic and Young's modulus of the intermetallic nanocomposite were also estimated. The biomedical and nanotechnology applications of nanocomposite intermetallic matrix application. The purpose is to demonstrate the possibility of obtaining single phase  $\beta$ -type Nb<sub>x</sub>Ti (x=50 at%) powders by ball-milling followed by FAST-SPS. The influence of milling parameters, and initial powders morphology have been studied. The produced powder can be further used to synthesize compacts with a very low Young's modulus for biomedical. To compare the properties/characteristics of Nb<sub>x</sub>Ti (x=50 at%) alloy and Nb<sub>x</sub>Ti (x=50 at%) reinforced SWCNTs fabricated using ball-milling and employing a better established method FAST-SPS. The properties/characteristics determined were phase composition, morphology, total porosity, inner pore architecture, compressive strength, compressive modulus, and in vitro biocompatibility. The in vitro biocompatibility, tribological properties and superconductivity measurement will be performed in the near future.

## Experimental Section

### Starting Material

In the present study, Niobium (Nb<3 $\mu$ m) and Titanium (Ti<5 $\mu$ m) elemental powders were used as initial material. High purity (~99.9% pure) Nb and Ti powders were supplied by Kojundo Chemical Laboratory Co. Ltd. (Japan). The FESEM micrographs of the as received Niobium (Nb) elemental Titanium (Ti), and SWCNTs produced by HiPCO process and by laser ablation method [47,48] with diameter of 1.0 nm (IFW-TU-Dresden-Germany) were used as the raw materials. The starting powders are shown in Figure 1. The Nb and Ti powder particles had an irregular shaped morphology together with both coarse- and fine-sized particles. Clearly, both the powders had comparable starting average particle size. Also, an X ray diffraction (XRD) analysis of the initial powders revealed that both the powders had cubic crystal structure not presented in this work.

### Mechanical Alloying

The equilibrium phase diagram of NbTi binary alloy system. The phase diagram shows that the  $\beta$ -phase allotropic phase transformation, for pure titanium, occurs at 1155 K. Since niobium acts as a strong  $\alpha$ -phase phase stabilizer, niobium additions result in a significant lowering of  $\beta$ -type phase transformation temperature. It can be seen that Nb-Ti binary alloys with more than 50 wt% Nb can retain the  $\beta$ -phase at very low temperatures. Therefore, to obtain  $\beta$ -type

phase stabilized Nb-Ti alloy, as received Ti and elemental Nb were blended together according to the desired optimum stoichiometric composition, i.e. 50 wt% titanium and 50 wt% Nb, Nb<sub>x</sub>Ti (x=50 at%) (further referred as Nb<sub>50</sub>Ti). The Nb and Ti powders were mechanically alloyed under argon atmosphere at room temperature, using planetary ball mill with stainless steel balls and vials-operating at a rotation speed of 200 rpm. To obtain homogenized and fine powder mixtures, the powder mixtures of Nb<sub>x</sub>Ti (x=50 at%) were ball-milled at a high speed of 200 RPM for 10 to 20 by using WC balls (diameter: 3 mm) and ethanol as the milling media. The ball to powder ratio was kept 6:1. To understand the microstructural evolution during ball-milling process, the mixture powder Nb and Ti samples were analyzed after mechanical milling time of 10 and 20 hours and then the powders mixture containing Nb<sub>50</sub>Ti were mixed with addition of 0.4 to 0.8 wt% of SWCNTs after preliminary treatment of SWCNTs was carried out to minimize the agglomerate of the added SWCNTs. Firstly; the weighed SWCNTs were immersed into acetone for about 5 h, and then were ultrasonically dispersed for 4 h. Secondly, the treated SWCNTs (0.4 to 0.8 wt% mixed with the former ball-milled blend Nb<sub>50</sub>Ti by magnetic agitation for 8 h and then ball milled for 10 h. The ball-milled intermetallic nanocomposites were prepared by wet milling in anhydrous alcohol for 3 h.

Finally, the powder mixtures with dispersed SWCNTs were dried by rotary evaporator under vacuum condition and were sieved to 70 mesh [49,50].

### Consolidation of Powders via Spark Plasma Sintering

The field assisted sintering Technics-Spark Plasma Sintering (FAST-SPS) method is an effective technique for the compaction of powder materials. A main characteristic of this method is the direct heating of the pressing tool and/or the sample by pulsed direct electrical current with low voltage. This results in high heating rates and allows for short treatment times in order to obtain highly compacted sinter bodies. The material transport (e.g. by diffusion) occurring during the sintering process can also be used for performing chemical reactions. Especially the conditions during the FAST-SPS process allow the use of the method also as an alternative synthesis route for intermetallic compounds, of which, some can be obtained only with difficulties by other techniques.

The intermetallic matrix nanocomposites ball-milled powders were consolidated via FAST-SPS-FCT method under high vacuum conditions using graphite die and punch at an applied external pressure of 60 MPa. In order to prepare high density compacts with negligible porosity, temperature and compression pressure was programmed to rise simultaneously, until stabilized to the maximum temperature and compression pressure, followed by holding the system at the same sintering conditions for 1.6 ks. Circular compacts with diameter 20 mm and thickness 4 mm were prepared using FAST-SPS-FCT. The sintering conditions used in this study are provided in Table 1. The sintering schedules are. In the FAST-SPS-FCT, machine temperature profile, punch displacement or shrinkage and displacement velocity are presented in the FAST-SPS FCT machine (Table 1 and Figure 2).

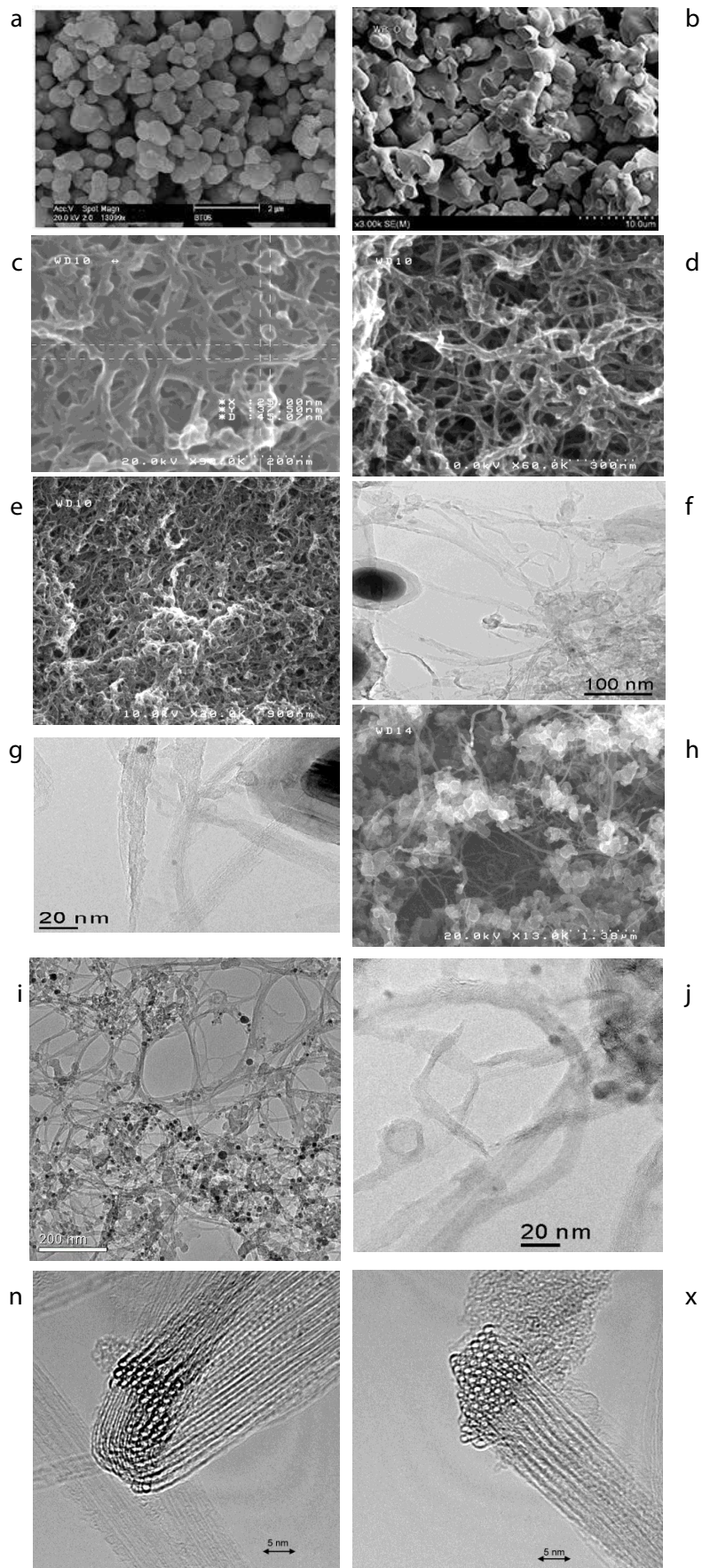


**Figure 1:** a-Ti powder morphology, b- Nb powder morphology, c, d, e, h- SEM of SWCNTs morphologies, f, g, j, k- TEM of SWCNTs with Fe catalyst, n, x: Bundles of SWCNTs.

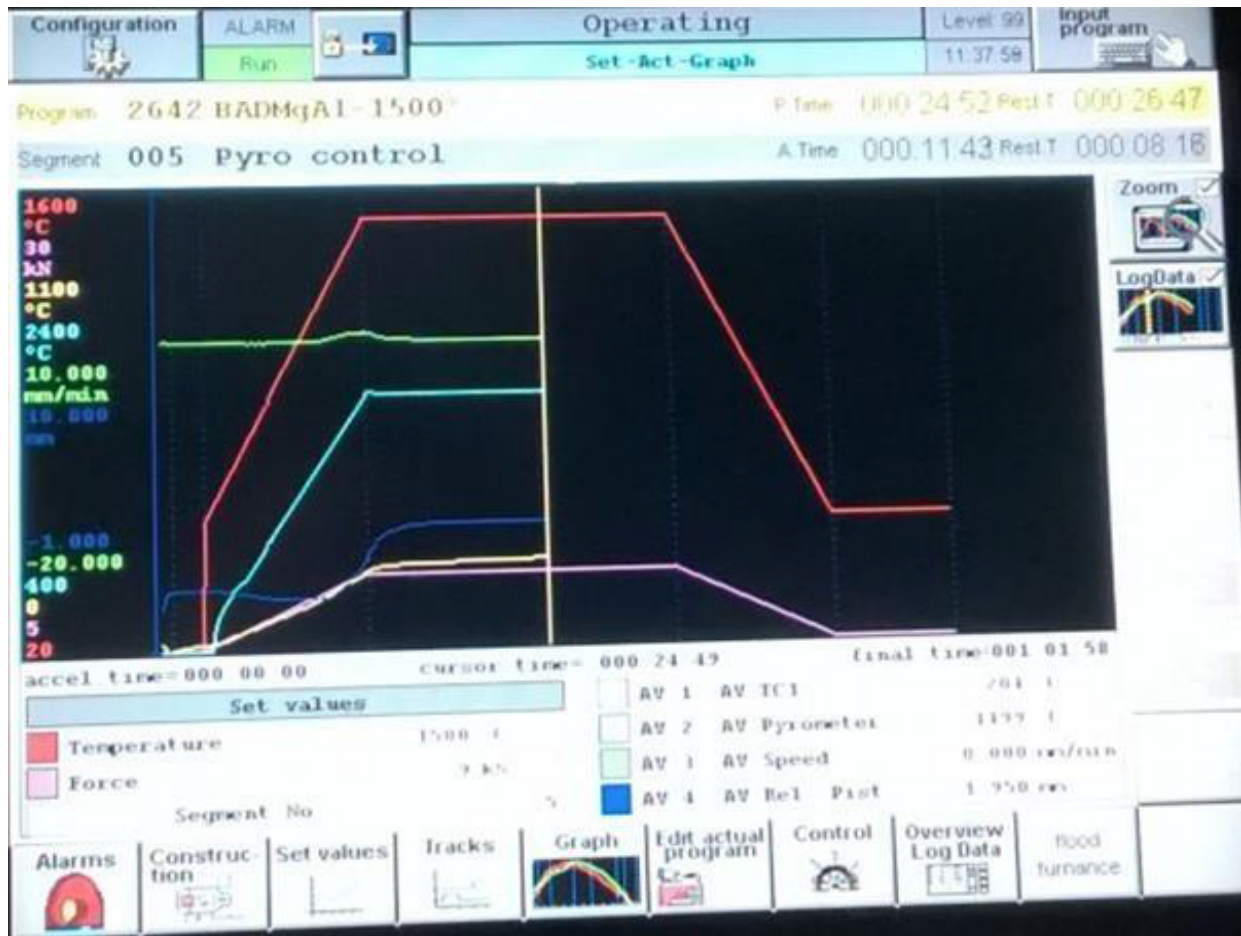


Figure 2: Variation of die displacement or shrinkage, temperature and applied pressure in dependence on the heating time during the FAST-SPS the sintered samples.

Table 1: FAST-SPS synthesis parameters.

Sintred Samples	T (°C)	Time of the cycle (mn)	Heating rate (°C/min)	P (MPa)	Ar (Sccm)	Wt.% SWCNTs d=1 nm	Current (A)
$\beta$ -type phase Nb <sub>50</sub> Ti	1200	10	100	70	200	00	3000
$\beta$ -type phase Nb <sub>50</sub> Ti/0.4 Wt% SWCNTs	1200	10	100	70	200	0.4	3000
$\beta$ -type phase Nb <sub>50</sub> Ti/0.8 Wt% SWCNTs	1200	10	100	70	200	0.8	3000

The resulting samples  $\beta$ -type phase Nb<sub>50</sub>Ti and  $\beta$ -type phase Nb<sub>50</sub>Ti/0.4-0.8 Wt% SWCNTs ultrafine powder mixtures were sintered by FAST-SPS in graphite dies (inner diameter of 20 mm) coated with graphite sheet lubricant atomized with cBN at 1273 to 1473°K in vacuum. Table 1 presented the sintering condition of intermetallic Nb<sub>50</sub>Ti and intermetallic nanocomposite Nb<sub>50</sub>Ti/SWCNTs 0.4-0.8. The applied pressure of 64 MPa was adjusted to the powder at room temperature and kept constant throughout the hot pressing process. The pressure was applied at the beginning of the sintering process because high green density is favorable for better densification rate by reducing the pores prior to the densification during heating. The heating rate was about 10°C/min and the dwelling time at terminal temperature was 60 min. The temperature was measured by an infrared pyrometer through a hole opened in the graphite die. Furthermore, for monitoring densification process, the shrinkage of the powder compact was measured by a displacement sensor during the sintering.

The dimensions of the finally sintered samples were about 20 mm in diameter and 3 mm in thickness after calculation of their weight using the densities values (Figure 3).

The mixtures were loosely compacted into a graphite die of 20 mm in diameter and sintered in the vacuum (1 Pa) at various temperatures using an FAST-SPS-FCT apparatus at the sinter Labs:

1. ENSICAEN, 6, Boulevard Maréchal Juin, CS 45053 14050 Caen Cedex 04, France.
2. Dipartimento di Ingegneria Chimica e Materiali, Università di Cagliari, Piazza d'Armi, 09123, Cagliari, Italy.
3. Tycho lab, Institut für Physik, universität Rostock Germany FAST-SPS-1050, Sumitomo Coal Mining Co. Ltd., Germany). A constant heating rate of 120°C/min was employed, while the applied pressure was 65 MPa. The on/off time ratio of the pulsed current was set to 10/2 in each run. The maximum current reached approximately 3000 A during sintering.

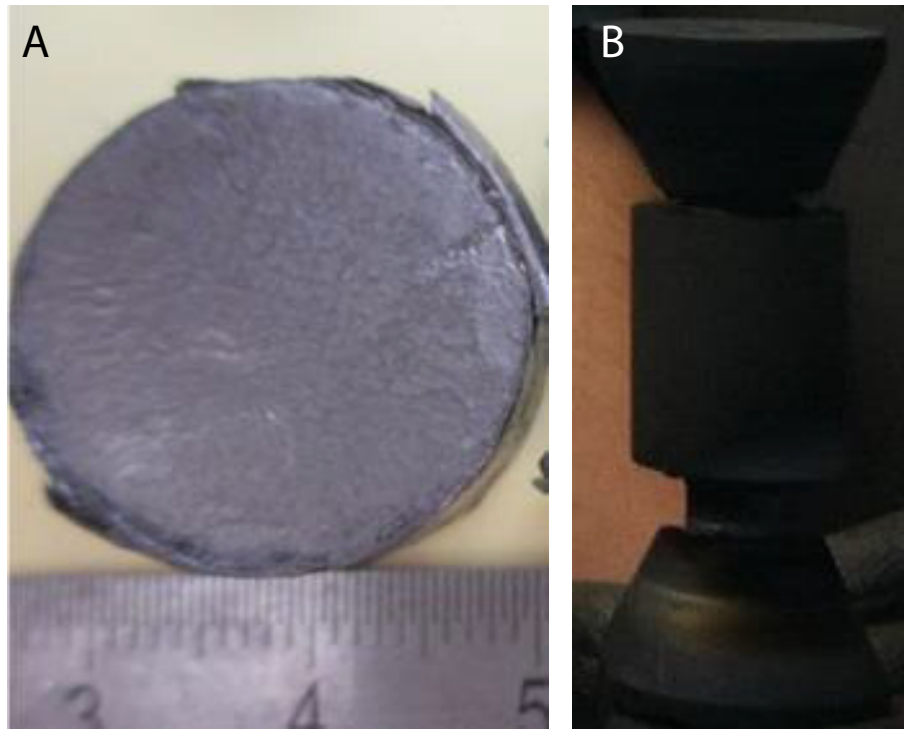


**Figure 3:** (a) Sintered samples in the die diameter of 20 mm of Nb50Ti /SWCNTs powder intermetallic nanocomposite. (b) Punch, die and spacer with 10 mm of diameter.

The soaking time at high temperatures was within 10 min. The upper ram of the FAST-SPS apparatus was fixed, while the displacement of the shifting lower press ram was recorded in order to analyze the synthesis and sintering. The sintered samples are presented in the Figure 3.

Density of the sintered samples was measured by the Archimedes' using the densimeter type Micromeritics Accucyc 1330.

### Mechanical Properties

Mechanical properties of the sintered compacts were evaluated the microhardness at the top were measured by a diamond Vickers hardness tester (MVK-H1, Meter-Mitutoyo, Japan).

The indentation loads, ranging from 2 to 500 N, were applied for 15 s for each measurement. The fracture toughness was measured using the Vickers indentation by the measurement of the producing failer.

In this study, 06 measurements for each sintering sample process were fabricated to obtain an average relative density and microhardness.

Young's modulus of the composites was determined by ultrasonic wave transition method measuring the velocity of ultrasonicsound waves passing through the material using an ultrasonic flaw detector (Panametrics Epoch III). The microhardness and the fracture toughness were determined by the Vickers indentation method applying load of 294 N (HV<sub>30</sub>) and 490 N (HV<sub>50</sub>), by a Future Tech FLC-50VX hardness tester. For each sample, 6 indentations were made and the stress intensity factor K<sub>IC</sub> was calculated from the length of Palmqvistcracks which developed during a Vickers indentation test

using E. Rocha-Rangel's equation.

The wear resistance and the friction coefficient (tribological behavior) will be performed in the near future. The hardness (H) and the toughness (K<sub>IC</sub>) of the manufactured samples were measured under ambient conditions using the instrumented Vickers indentation method (ZwickRoell, ZHU 2.5 apparatus). The impression diagonal (2a) was measured, and the hardness values were calculated according to the following relation:

$$H_v = (1.8544 * F) / (2a)^2 \quad (1)$$

The fracture toughness was also calculated by indentation fracture (IF) method according to the equation:

$$K_{IC} = 0.16 H_v a^{1/2} (c/a)^{-3/2} \quad (2)$$

Where H<sub>v</sub> was the Vickers hardness, a was the half-length of the indentation diagonal and c was the half-length of the median crack generated by indentation. Generally, the fracture toughness measured by IF method were fluctuating values with relatively large deviations due to the phase distribution and measurement errors of calculation. Thus a linear regression model was applied to get a reliable value of indentation fracture toughness.

To obtain the values of A, B and R<sup>2</sup>, a series of indentation loads (10 N, 50 N, 100 N, 300, 500 N) were applied to get the relations of P and c<sup>3/2</sup>

Where P was the indentation load. Through the combination of equations (1) and (2), the linear relation between P and c<sup>3/2</sup> was obtained:

$$P = A c^{3/2} + B \quad (A = K_{IC} / 0.075) \quad (3)$$

A linear regression analysis was applied to the relations of P and  $c^{3/2}$  by the least square method. Where A was the slope, B was the intercept. To obtain the values of A and B.

In addition, a high determination coefficient ( $R^2$ ) was obtained through the linear regression model. Hence, when combined with the linear regression model, IF was shown to be an effective method in the evaluation of fracture toughness for its convenience and material saving. The compressive strength and the compressive modulus of elasticity of the produced alloy and nanocomposite were determined from compression tests carried out on the cylinders, at room temperature, at a strain rate of  $10^{-3}\cdot s^{-1}$ .

*In vitro* biocompatibility experiments to be performed using human bone marrow stromal cells (hBMSC). For isolation of hBMSC, bone marrow aspirates will be collected from bone marrow donors (age:  $32 \pm 3$  years) at the CHU-Bone Marrow Transplantation Centre Hospital ibn Rochd-Annaba-Algeria to the laboratory.

The study will be approved by the local ethics commission. The donors will be informed and gave their approval. hBMSC were isolated using the method described by.

Bone marrow aspirate will be diluted 1:5 with 0.5% human serum albumin (HSA) in phosphate-buffered saline (PBS) and applied to a Percoll density gradient ( $d=1.073$  g/mL). After centrifugation at 900 g for 30 min at 25°C, mononuclear cells in the interface will be harvested and filtered through a nylon cell strainer. The cells will be re-suspended in DMEM containing 10% heat-inactivated fetal calf serum FCS and antibiotics. After 24 h, non-adherent cells were removed. When the adherent cells reached about 90% confluence, they were trypsinized with 0.05% trypsin/0.02% EDTA (v/v) in PBS and sub-cultured. For the experiments, 5000 hMSC/cm<sup>2</sup> were deposited on the test specimen. Metabolic activity was determined by the MTS assay (Cell Titer 96 Aqueous One Solution Proliferation Assay) 24 h after plating.

Conditioned medium was replaced by fresh medium containing 10% of MTS dye solution. After 2 h of incubation at 37°C in a humidified CO<sub>2</sub> incubator, 80 mL cellular medium was transferred to a 96-well plate and the absorbance of the formed MTS formazan dye will be measured photometrically at 490 or 655 nm.

In terms of statistics, the results of the quantitative parameters are presented as mean  $\pm$  standard deviation (together with median and variance, in some cases). Significance of difference of the pT, ultimate compression strength, and compressive modulus of elasticity results between the two study groups was performed using the Mann-Whitney test, with significance denoted at  $p < 0.05$ . The superconducting measurement of critical temperature, critical current density and critical magnetic field on the nanocomposites samples for the superconducting magnet in ITER apparatus.

## Results and Discussion

### Phase and Microstructural Analysis

The general phase analysis was carried out at ambient temperature by XRD analysis with a CuK $\alpha$  ( $\lambda=1.5406$  Å) source at 40 kV voltage and 30 mA current. The microstructural characterization of the initial powders, ball-milled powders, and consolidated compacts was carried out by FESEM equipped with back scattered electron (BSE) and electron back scattered diffraction (EBSD) facilities. Primary chemical characterization was carried out by Energy Dispersive X-ray Spectroscopy (EDS) technique. The diameter of single consists of  $\beta$ -type phase Nb<sub>50</sub>Ti about  $24 \pm 2$   $\mu$ m. The XRD pattern taken from the cross-section of the sintered samples is shown in Figure 4. Both a main  $\beta$ -phase and a minor  $\alpha$ -phase are identifiable. The amount of  $\alpha$ -phase was evaluated as  $10 \pm 2\%$  by the Le Bail method. The appearance of  $\alpha$ -phase can be mainly attributed to a slow cooling rate as the samples had to be cooled inside of FAST-SPS-FCT chamber. After slow cooling, the presence of the  $\omega$  phase precipitates (hexagonal

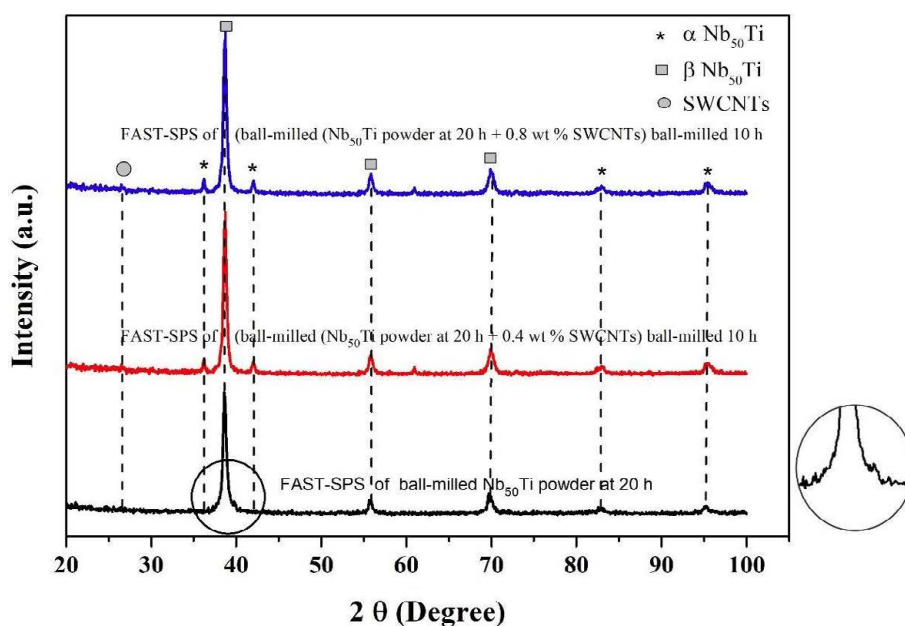


**Figure 4:** X-ray diffractometer (XRD), patterns of blue line, FAST-SPS of (ball-milled (Nb<sub>50</sub>Ti powder at 20 h + 0.8 wt% SWCNTs) ball-milled 10 h. Red line, FAST-SPS of (ball-milled (Nb<sub>50</sub>Ti powder at 20 h + 0.4 wt% SWCNTs) ball-milled 10 h. Black line FAST-SPS of ball-milled Nb<sub>50</sub>Ti powder at 20 h. A higher resolution of its (101) peak.

structure, space group P6/mmm) is also possible because, according to the literature data  $\omega$ -phase precipitates may form during a slow quenching from the  $\beta$ -type phase region or during isothermal aging. The presence of the  $\omega$ -phase is hard to detect from the XRD patterns but it was confirmed by TEM studies in a previous work [51-53].

The XRD patterns of the pre-mixed and ball-milled Nb<sub>50</sub>Ti powder mixtures (ball-milled from 10 to 20 hours) are shown in Figure 4a. These XRD patterns were compared with the JCPDS data of the oxides of Ti and Nb. No visible oxide peaks were found to be present in the XRD patterns of the ball-milled powders, indicating the absence of any substantial quantity of oxides. However, an analysis of the XRD profiles clearly shows a broadening of peaks with increasing milling time from 10 to 20 h. Sample made by FAST-SPS-FCT of intermetallic nanocomposite  $\beta$ -type phase Nb<sub>50</sub>Ti/0.4-0.8 Wt% SWCNTs ball-milled powder. At the Figure 4 is represented the higher resolution of its (101) peak.

Figure 4a shows the XRD profiles of the ball-milled powders compacts sintered at 1473°K. These patterns depict and illustrate the microstructural/phase evolution at the sintering temperature. It can be clearly observed that the sintering temperatures led to almost formation of various new alloy phases such as Ti-rich  $\alpha$ -type phase, and  $\beta$ -type phase. In particular,  $\alpha$ ,  $\beta$ -type phase, and pure niobium were formed at lower temperatures.

Ball-milled powder was sieved to select particle sizes of  $20 \pm 2 \mu\text{m}$  and its flowability was determined to be very good. Therefore, the ball-milling produced powder was found to be suitable for use in FAST-SPS-FCT. The broadening of the peaks in the XRD spectra at different stages of the ball-milling process suggests the formation of an ultrafine grain structure and an accumulation of strain in the lattice, which is typical for ball-milling related to severe mechanical deformation [54]. The ball-milling process, the morphology and phase composition of the powder were discussed in detail in the previous work of the authors (Figures 4 and 4a).

## Structural and Morphological Characterization

To acquire the information on the distribution of various phases in the sintered samples, Energy-Dispersive X-ray Spectroscopy (EDS) analysis was performed on the samples. Although it is not possible to identify the phases by EDS directly, it is still very useful to detect elemental distribution of Nb, Ti and SWCNTs in samples. Thus, EDS analysis together with XRD results can provide more information regarding nature of FAST-SPS of compact powder.

The FESEM images and their corresponding elemental distribution maps of previous ball-milled and then FAST-SPS powders at  $T=1473^\circ\text{K}$  are shown in Figure 5a. Figure 5b shows the morphology, and their corresponding elemental distribution, of the powder mixture (Nb, Ti, SWCNTs).

Zhang et al. [55] has reported that cold welding and severe plastic deformation is the dominant mechanism which operates during mechanical milling of ductile Nb powder particles. Due to severe plastic deformation and cold-welding, Nb particles become hard and brittle, leading to their fragmentation during subsequent mechanical milling. As a result, relatively coarser Nb particles are obtained in the ball-milled powder mixture. It would also be worth mentioning that such a deformation and fracturing of particles leads to the formation of niobium particles with energetically activated surface. FESEM images and their corresponding elemental distribution maps phase evolved as the major phase in the sintered compacts and the intensity of the peaks corresponding to the  $\beta$ -type phase increased with increasing amount of SWCNTs at the sintering temperature. Finally,  $\beta$ -type phase appeared to be the major phase formed in the compacts sintered at 1473°K. They consisted of primarily beta phase together with extremely small amounts of alpha phase. Microstructure of the Nb<sub>50</sub>Ti alloy intermetallic ball-milled 20 h compacts sintered at  $T=1473^\circ\text{K}$  is illustrated in Figure 5a through typical FESEM micrographs collected in back scattered electron (BSE) mode. The sintered Nb<sub>50</sub>Ti and intermetallic nanocomposite Nb<sub>50</sub>Ti/SWCNTs samples exhibited

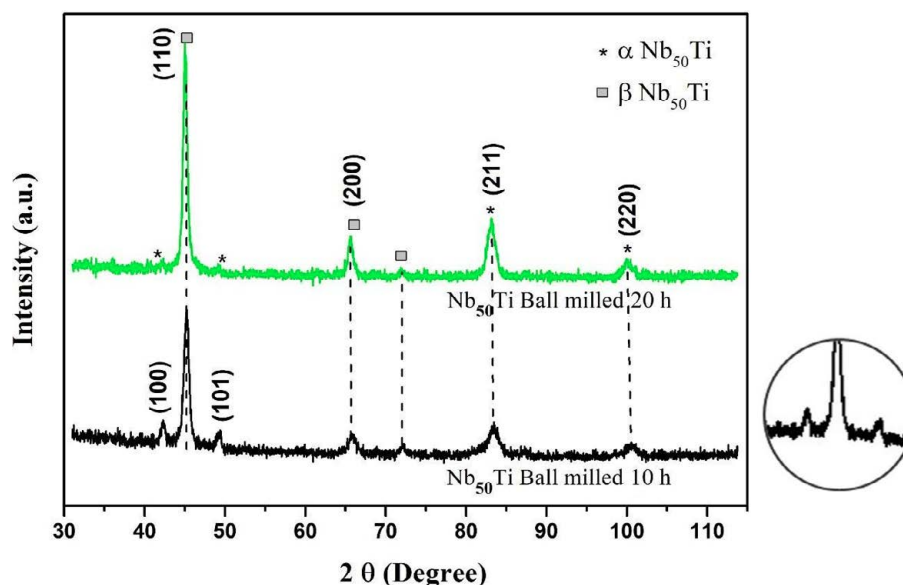
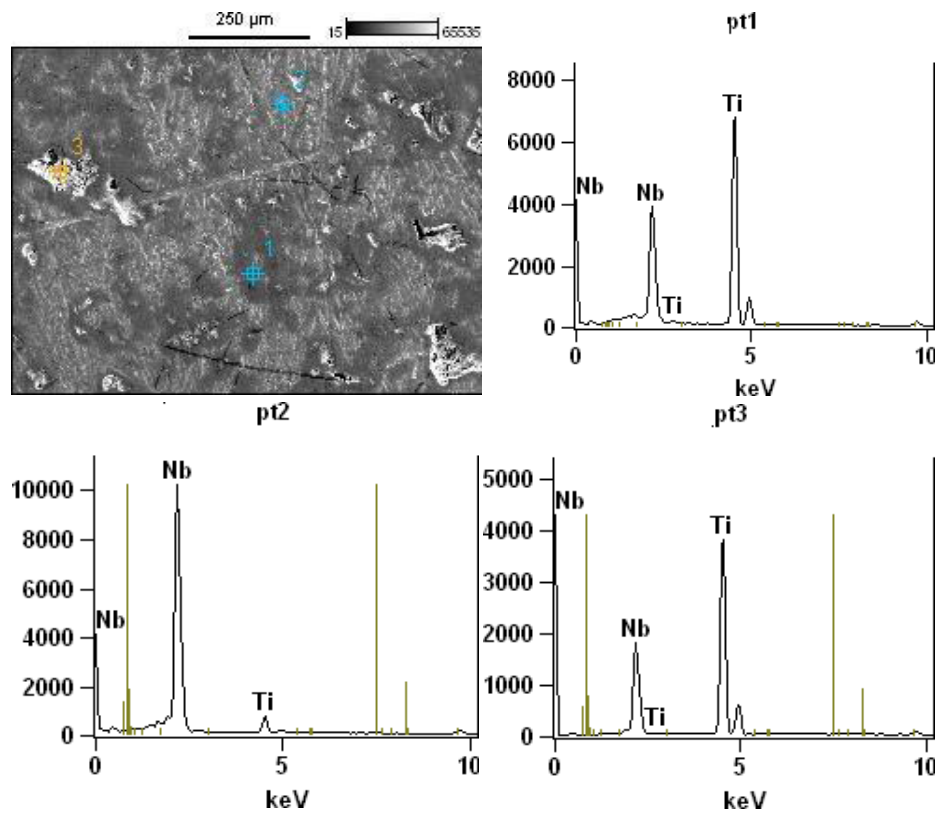
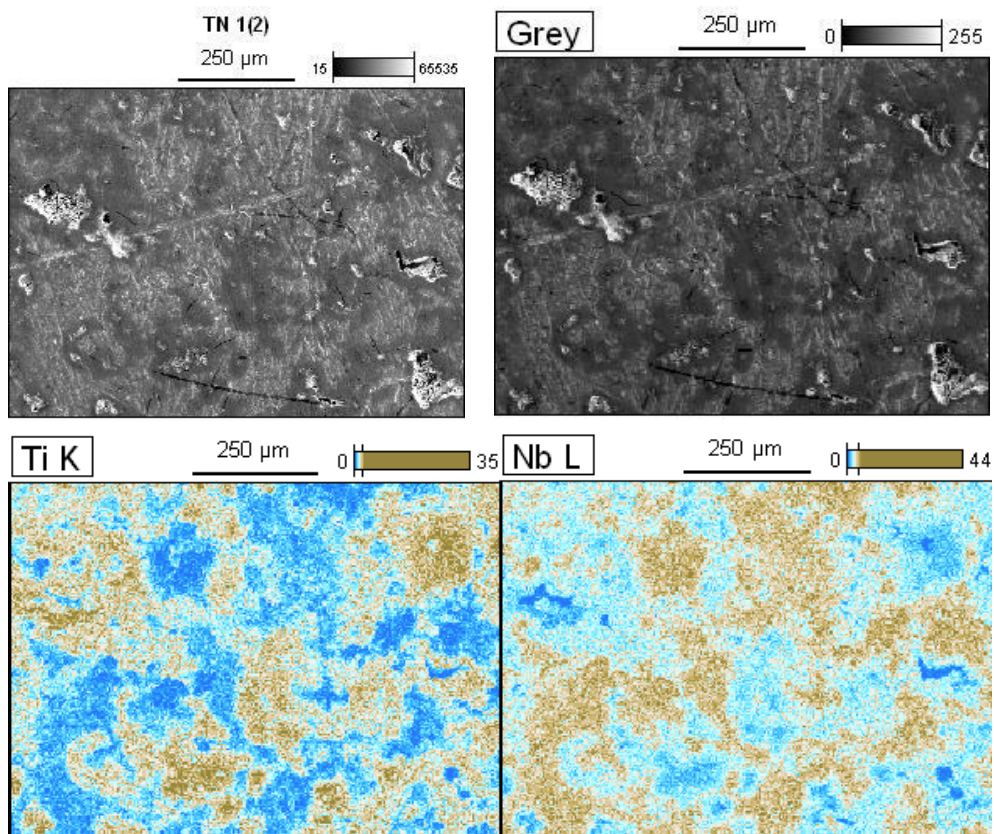


Figure 4a: X-ray diffractometer (XRD) patterns of green line Nb<sub>50</sub>Ti ball-milled 20 h. Black line Nb<sub>50</sub>Ti ball-milled 10h. A higher resolution of its (101) peak.



**Figure 5:** High magnification micro structural representative FESEM image and EDS spectra obtained on three different regions of the surface of the sample made of Nb50Ti ball-milled 20 h and sintered at T=1473°K.



**Figure 5a:** High magnification micro structural representative FESEM image and corresponding elemental distribution maps (Nb, Ti) of a previous sample of Nb50Ti ball-milled 20 h of polished and etched surface sintered at T=1473°K.

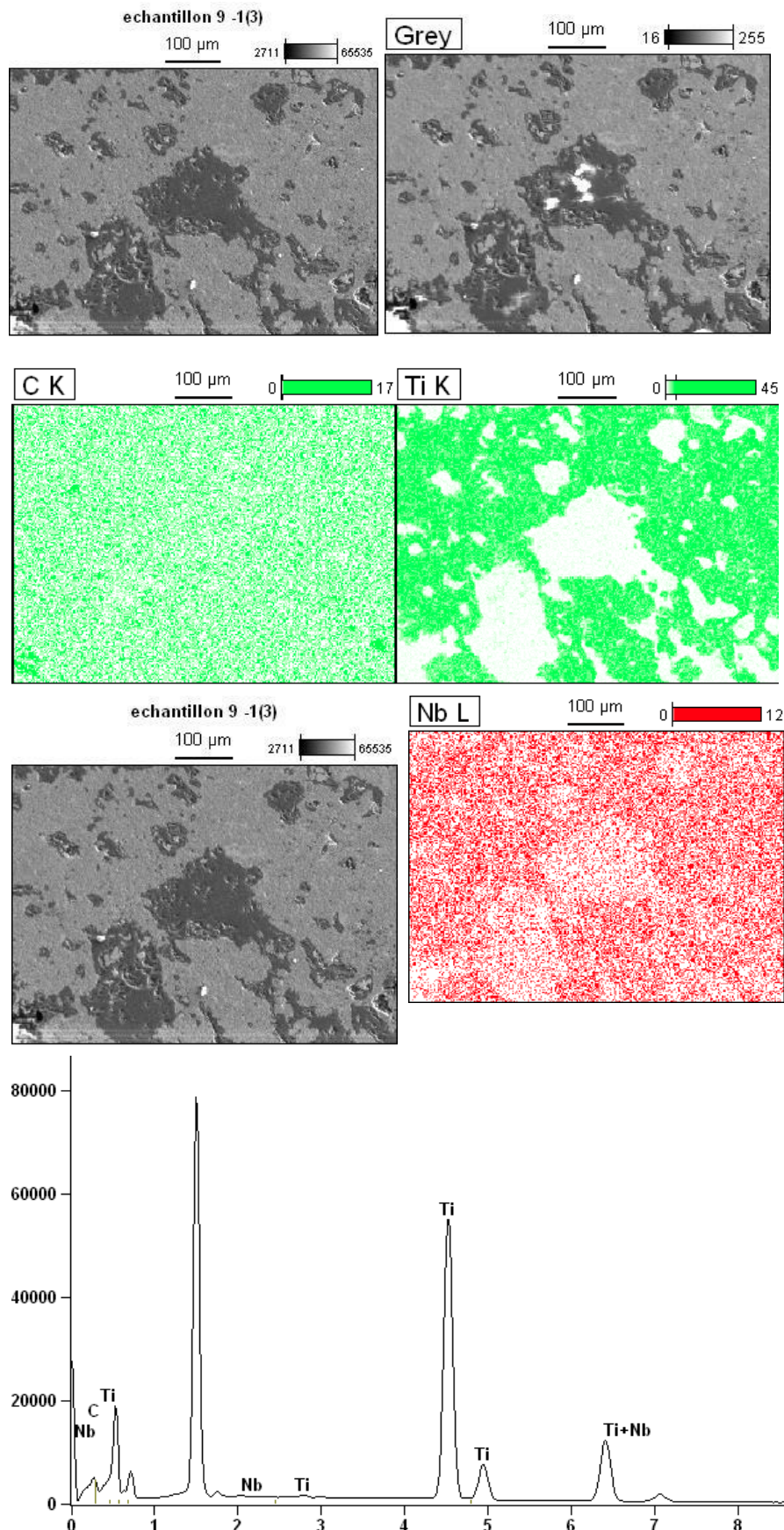


**Figure 5b:** High magnification micro structural representative FESEM image their corresponding elemental distribution maps (Nb, Ti and C) of FAST-SPS (ball-milled Nb<sub>50</sub>Ti powder at 20 h + 0.8 wt% SWCNTs) ball-milled 10 h of polished and etched surface sintered at T=1473°K. Its higher resolution global analysis EDS pics is presented.

very high density, approximately 94%, with appearance of minimum porosity. The microstructure of low-temperature sintered (1473°K) Nb40 Ti intermetallic alloy compacts (Figure 5a) show three different color composition: (I) bright colored phase, which is the pure Nb phase as verified by energy dispersive X-ray spectroscopy (EDS) analysis and contains Nb and Ti; (II) grey-colored phase, which is the  $\beta$ -type phase and contains Nb50Ti; and(III) comparatively dark-colored phase, which is the  $\alpha$ -phase and contains Nb50Ti. Similarly, the microstructure of the Nb50Ti/0.8 wt% WCNTs intermetallic nanocomposite compacts sintered at moderate temperature (1473°K), as shown in Figure 5b, also demonstrated three different phases similar to the ones observed in the low temperature sintered Nb50Ti compacts. It can be observed that, the fraction of the bright and the dark phases decreased whereas the fraction of the grey phase increased in the matrix with increasing of amounts of SWCNTs from 0.4 wt% to 0.8 wt%, which could be attributed to the increased inter-diffusion of Ti and Nb and SWCNTs at the sintering temperature. The EDS analysis clearly demonstrated that the grey phase corresponds to the  $\beta$  type phase composition. Therefore, the above results clearly show that the lower sintering temperature result  $\beta$  type phase rich Nb50Ti intermetallic alloy with increased homogeneity. Clearly, these results are in conformity with the phase evolution as observed via XRD results, as already shown in Figure 4.

The FESEM represented separately each  $\alpha$ -phase and  $\beta$ -type phase. For Nb50Ti compacts sintered at 1473°K, the calculated average grain size for  $\alpha$  and  $\beta$ -type phase was  $2.9 \pm 1.02 \mu\text{m}$  and  $9.61 \pm 4.20 \mu\text{m}$ , respectively (Figures 5a and 5b).

Finally, the average grain size  $\alpha$ -type phase and  $\beta$ -type phase of Nb50Ti/0.8 wt% SWCNTs intermetallic nanocomposite compacts sintered at 1473°K was  $1.75 \pm 0.4 \mu\text{m}$  and  $4.75 \pm 0.83 \mu\text{m}$ , respectively, in the Figure 6 is presented the homogenous distribution of carbon nanotubes (Figure 6).

High magnification micro structural representative FESEM image sample of Nb50Ti ball-milled 20 h of polished and etched surface sintered at T=1473°K, showing the precipitates embedded in the  $\beta$ -type phase matrix intermetallic nanocomposites (Figure 7).

These results clearly demonstrate that fine-grained  $\beta$ -type phase Nb50Ti intermetallic alloy and its nanocomposite based on SWCNTs can be successfully prepared via present processing technique FAST-SPS after sequentially ball-milling wherein the high yield of the material with good density and defined porosity remains ensured for biomedical and nanotechnologies applications by FAST-SPS method.

## Mechanical Testing

### Mechanical Properties

#### Density and Porosity of Sintered Samples

The theoretical density of the nanocomposite used for obtaining relative density was calculated using a rule of mixture, using the densities of two constituent phase (Nb50Ti=6 5.7 g/cm<sup>3</sup>,  $\rho$ SWCNTs=2.25 g/cm<sup>3</sup>) with the given FAST-SPS processing parameters, the Nb50Ti without addition of 0.4 to 0.8 wt% SWCNTs sample exhibited best densification with relative density greater than 94.5%, with the similar processing parameters with addition of SWCNTs. The relative density increases with the addition of SWCNTs. The Nb50Ti with addition of 0.4 to 0.8 wt% SWCNTs intermetallic nanocomposites at T=1200°C exhibited relative density of about 97.2%. Depending on the final density to be achieved, the FASY-SPS operating condition were properly chosen, that is, 1200°C, 75 MPa for 10 min, to obtain a highest relative density for the intermetallic nanocomposites for 7, 23, and 2.8% compacts porosity, 94.5, 97.06 and 97.6, respectively.

The porosity (pT) for the FAST-SPS fabricated cylinders was 7%  $\pm$  1% (median=7.0%; variance: 0.4%), which is in good agreement with the value obtained using density determined by simply dividing the mass of the cylinder by its volume for Nb50Ti for biomedical application. The porosity is mainly formed by spherical pores, which result from the gas uptake by the powder during the ball milling process. These spherical pores and such a relatively low porosity are typical for alloys fabricated using FAST-SPS.

For FAST-SPS cylinders, the size of the micropores and pT were 3–12  $\mu\text{m}$  and 3 -2.6%  $\pm$  0.4% (median=3.0%; variance=0.06%), for Nb50Ti with addition of 0.4 to 0.8 wt% SWCNTs which is in good agreement for biomedical application (Table 2 and Figure 8).

#### Vickers Microhardness of Sintered Samples

Hardness values were measured on the bulk Nb50Ti alloy and its nanocomposite based SWCNTs compact samples sintered at T=1473°K. The variation in the hardness with the amounts of SWCNTs at sintering temperature is shown in Figure 9. It can be seen that the average hardness increases significantly with increase in the amounts of SWCNTs from 0.4 to 0.8.

Nevertheless, it would be worth noticing that the hardness of the specimens with coarser grain size and higher amounts of softer  $\beta$ -type phase demonstrates higher average hardness values as compared to those having relatively harder  $\alpha$  phase. Interestingly, it can also be

**Table 2:** Basic physical–mechanical properties of the samples obtained by ball-millig and then FAST-SPS.

Sintred samples	$\beta$ -type phase Nb50Ti	$\beta$ -type phase Nb50Ti/0.4 Wt% SWCNTs	$\beta$ -type phase Nb50Ti/0.8 Wt% SWCNTs
Relative density (g/cm <sup>3</sup> ) (%)	94.04	97.06	97.6
Young's modulus (relative Young's) (GPa)	60	62	64
Compressive elastic strainingh (MPa)	620	630	650
Compressive elastic modulus (MPa)	124	126	130
Porosity (pT) (%)	7	3.0	2.8

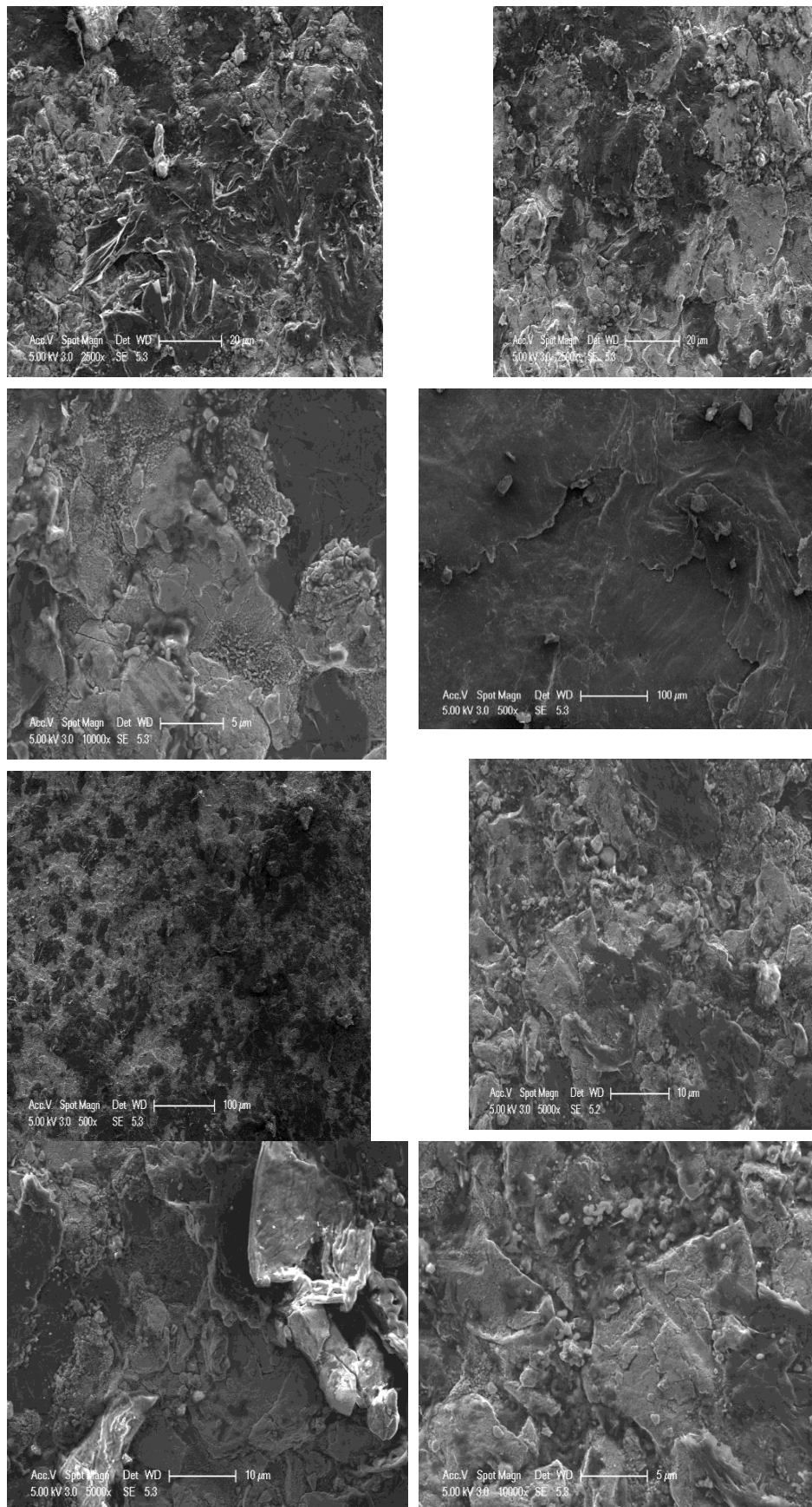


**Figure 6:** High magnification micro structural representative FESEM of FAST-SPS (ball-milled Nb<sub>50</sub>Ti powder at 20 h + 0.8 wt% SWCNTs) ball-milled 10 h of polished and etched surface sintered at T=1473°K.

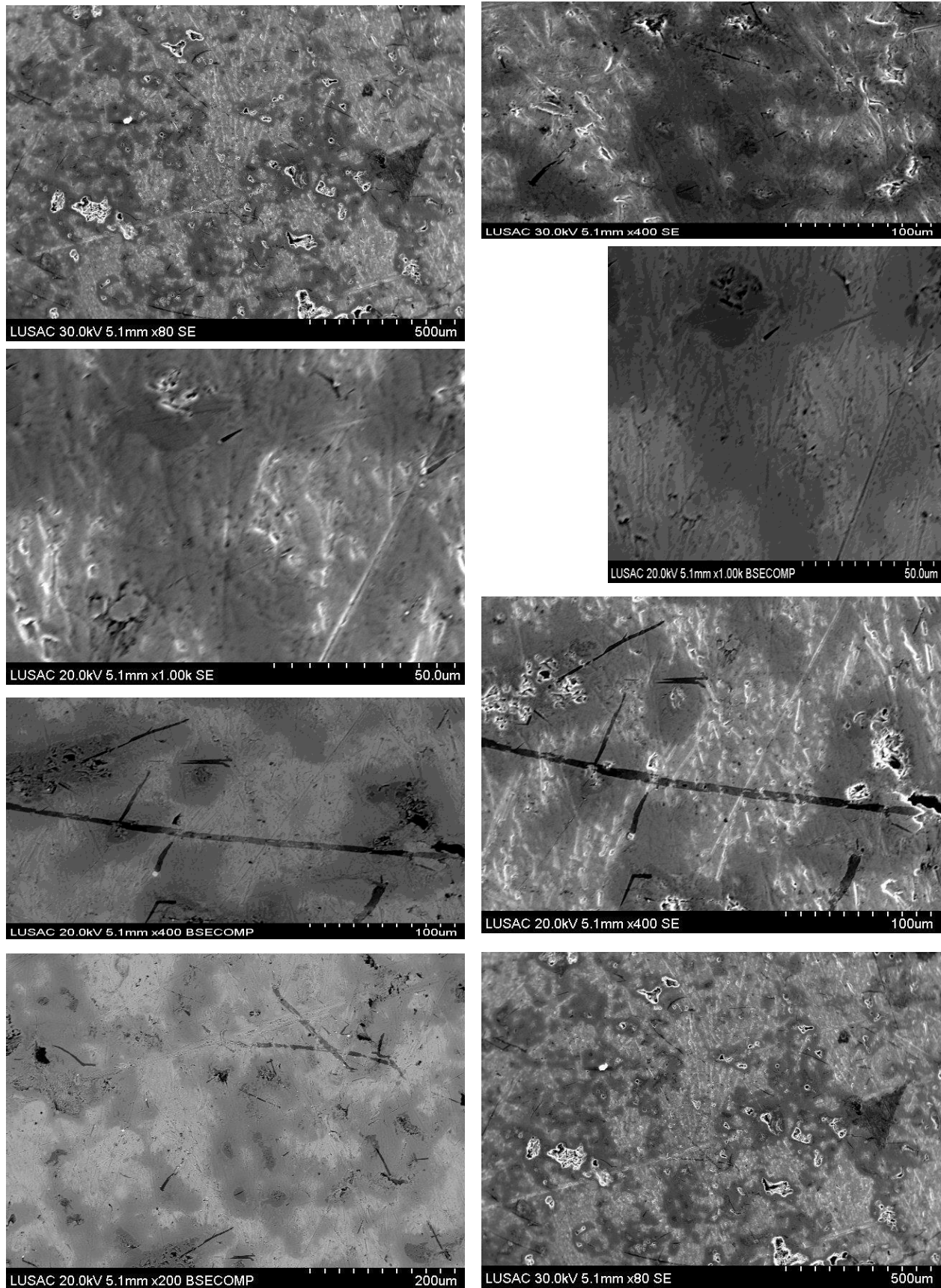


**Figure 7:** High magnification micro structural representative FESEM image sample of Nb<sub>50</sub>Ti ball-milled 20 h of polished and etched surface sintered at T=1473°K, showing the precipitates embedded in the  $\beta$ - type phase matrix.

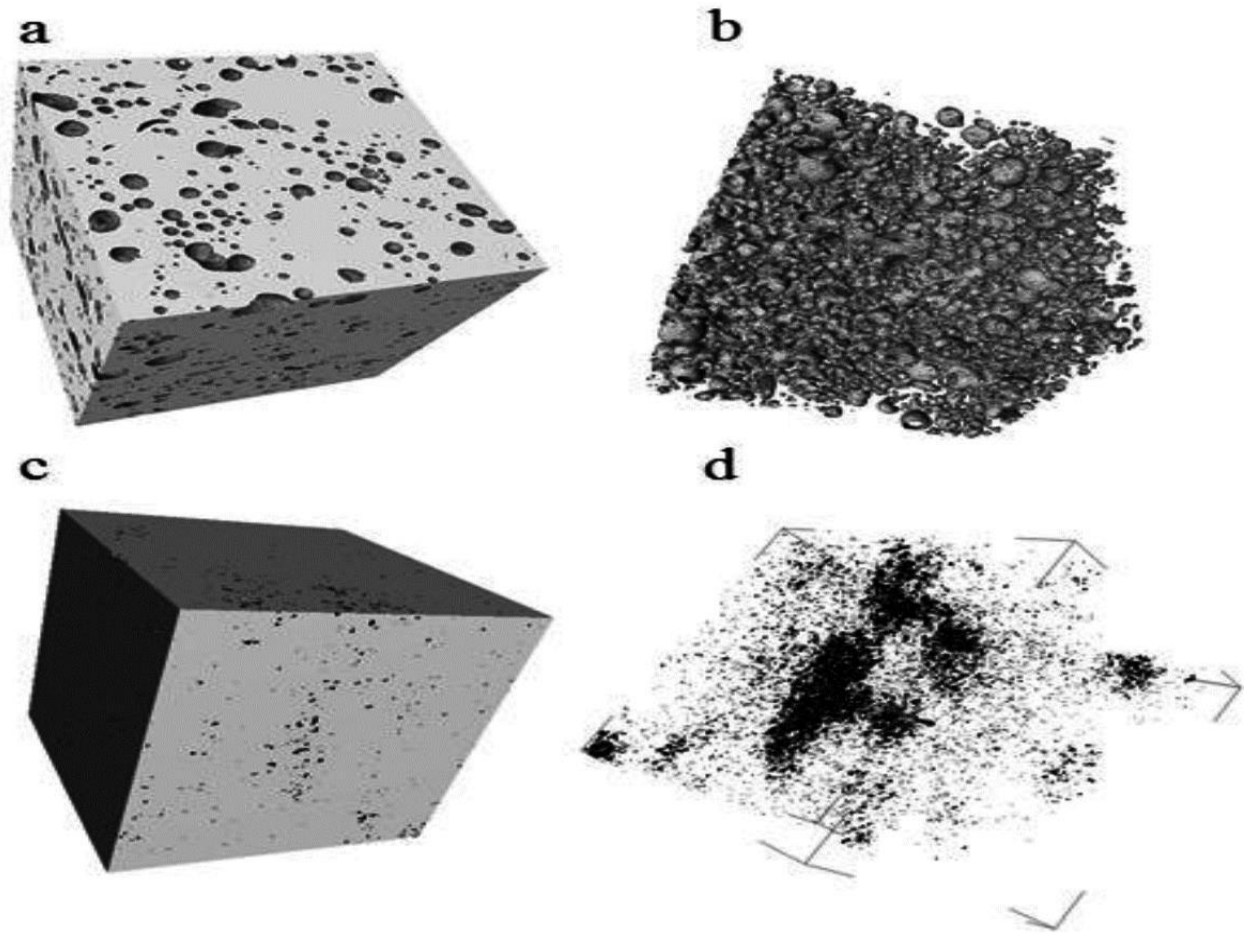


**Figure 8:** Micro-computed tomography ( $\mu$ CT) images of (a) sample manufactured by FAST-SPS of (ball-milled (Nb<sub>50</sub>Ti powder at 20 h + 0.8 wt% SWCNTs) ball-milled 10 h. (b) its inner porous architecture (from image analysis); (c) sample made FAST-SPS of ball- milled Nb<sub>50</sub>Ti powder at 20 h. (d) its inner porous architecture (from image analysis).

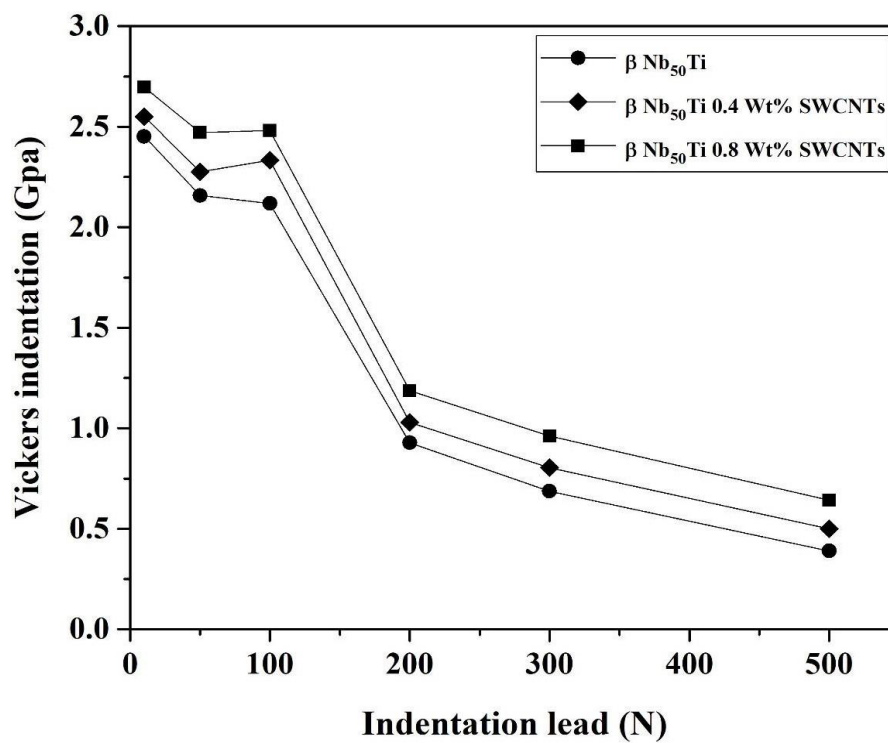


**Figure 9:** Representation of the variation of Vickers micro hardness function of the indentation leads of the sintered samples using a 20-mm.

observed that the standard deviation decreased from 2.35 to 2.65 Gpa (Table 2) with increasing of amounts of SWCNTs. These results can be explained with respect to the volume fraction of various phases and homogeneity of microstructures. The average hardness of any specimen is essentially an average of the hardness of these individual phases coupled with volume fractions resulting in better mechanical properties and ductility.

According to the above results, it can be concluded that the Vickers hardness has been improved by adding SWCNTs and enhanced with the fracture toughness value giving a better ductility and defined porosity for the reinforced  $\beta$ -type phase samples for bio-application. With this addition in the matrix, the electro discharge among powders may lead to self-heating and purification of the particle surface, resulting in activation of the formation of the nanocomposites. The addition of SWCNTs plays an important binder less role (the ductility) in the propagation of failer in this nanocomposites and thus enhance the fracture toughness in comparison with his higher hardness.

### Fracture Toughness (KIC) of Sintered Samples

Niobium is known by his ductility and superconductivity. In this context we proceeded to the determination of the tenacity of the sintered samples as well as the determination of the parameters associated with this calculation. But unfortunately we could not determine the critical cracking load due to ductility of the sintered samples.

### Vibronic Properties

#### Raman Spectroscopy Analysis

To verify the XRD experimental results Raman spectroscopy is a powerful technique for characterizing degree of disorder of CNTs. SWNTs with a Raman spectroscopy measurement of 513.5 nm were studied. In general, Raman spectroscopy can observe the distribution of dielectric bonding SP3, D band and metallic bonding SP2, G band [55-61].

Different regions of the sample. In Figure 10 is presented which

depicts the absence of radial breathing mode (RBM), which is attributed to the absence of SWCNTs. The first-order Raman spectra of MWCNTs has a small peak at  $1364\text{ cm}^{-1}$  and strong peak at  $1590\text{ cm}^{-1}$ . A band at  $1364\text{ cm}^{-1}$  (D) arises due to the presence of disorder in the carbon system as well as breathing of hexagons at border of crystalline areas of nanoparticles and fine crystallite. A sharp and narrow high-intensity band occurred at  $1590\text{ cm}^{-1}$  (G band) which approved high crystallinity of graphite and graphitic structure of graphene. 2D or G-band peak at  $2705\text{ cm}^{-1}$  and at  $2720\text{ cm}^{-1}$  for second order of D band. They investigated that 2D band peak of synthesized graphene have no shoulder, which corroborates the characteristics of graphene with few layers which is a characteristic of graphene with more layer and ascribed to the overtone of first-order D band ( $1364\text{ cm}^{-1}$ ).

The ratio of D band and G band demonstrates the degree of disorder induced in bulk samples. If both bands have equal intensity, then there is a high degree of disorder in the bulk samples. The relations among D band, G band and RBM play predominant role to distinguish between different variants of CNTs.

The experimental results are shown in Figure 10. The peak positions of SWCNTs were similar, but the ratios of the D band  $1380\text{ cm}^{-1}$  and the G band  $1590\text{ cm}^{-1}$  were quite different and collective excitation of  $\beta$ -type phase from the difference in the ratios, it was found that region 1 have higher dielectric properties than region 2 (Figure 10) because SWCNTs have underwent a transformation during heating of sintering to DWCNTs or MWCNTs in high vacuum.

To analyze these experimental results qualitatively, we modeled the composite system which is composed of CNTs nanoparticles in Nb<sub>50</sub>Ti host medium. The CNTs have both metallic and semiconducting properties (region 3 and 4) (Figure 10a) because they consist of diverse nanotubes and contact junctions [62,63].

Describing these properties, the dielectric function of CNTs ( $\epsilon$ CNTs) CNTs can be represented as a combination of the Drude and Lorentz harmonic oscillator models [64] (Figures 10 and 11).

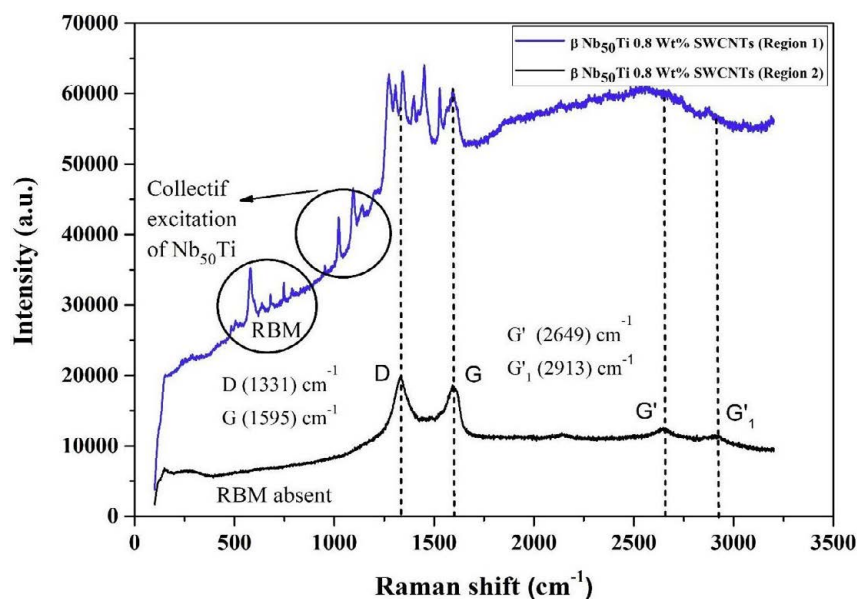


Figure 10: Raman spectra of FAST-SPS (ball-milled Nb<sub>50</sub>Ti powder at 20 h+0.8wt% SWCNTs) ball-milled 10 h of polished and etched surface sintered at T=1473°K (region 1 and 2).

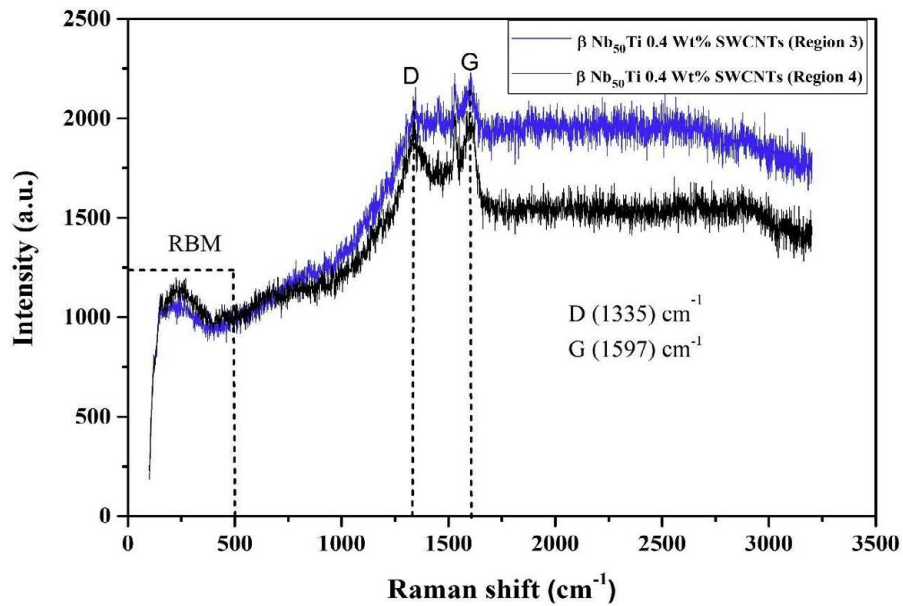


Figure 10a: Raman spectra of FAST-SPS (ball-milled Nb<sub>50</sub>Ti powder at 20h + 0.8wt% SWCNTs) ball-milled 10 h of polished and etched surface sintered at T=1473°K (region 3 and 4).

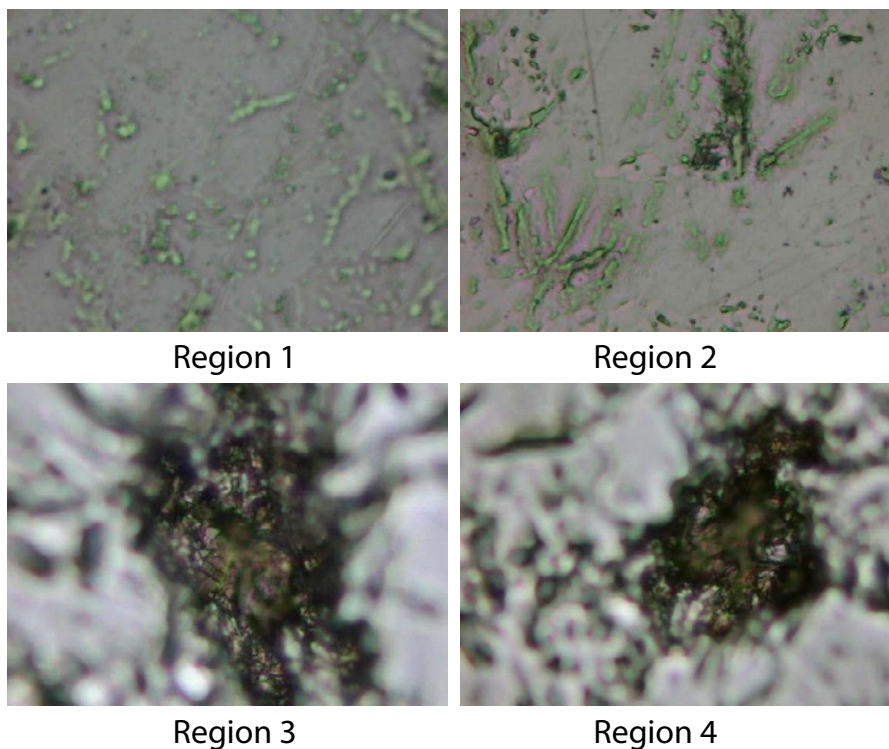


Figure 11: Raman images caption, region 1 and 2 corresponding to carbon nanotubes and  $\beta$ -type phase Nb<sub>50</sub>Ti. The region 3 and 4 correspond to carbon nanotubes.

## Conclusions

In this study, intermetallic alloys fine-grained  $\beta$ -type phase matrix Nb<sub>50</sub>Ti/SWCNTs nanocomposite was successfully prepared by ball-milling of titanium elemental niobium and SWCNTs powders followed by spark plasma sintering. The final ball-milling (Nb<sub>50</sub>Ti/SWCNTs) resulted in a very high yield of milled powders, the powder had micron-sized Nb<sub>50</sub>Ti and a nano-sized (Nb<sub>50</sub>Ti/SWCNTs).

After the FAST-SPS the obtained material was a small amount of  $\alpha$

and major  $\beta$ -type phase. The microstructure and the phase evolution in the sintered Nb<sub>50</sub>Ti compacts depend on the SWCNTs addition because now diffusion between Nb, Ti and SWCNTs was not observed, and almost complete  $\beta$ -type phase was achieved after sintering at 1473 K. Spark plasma sintering demonstrated the capability to yield fine grained microstructure even after sintering at low temperatures. The grain size of the synthesized Nb<sub>50</sub>Ti strongly depends on the on the SWCNTs addition, i.e. the grain size of  $\alpha$  and  $\beta$ -type phases increases with of amounts of SWCNTs.

Compressive strength and modulus of the FAST-SPS-manufactured  $\beta$ -type phase were  $620 \pm 6$  MPa and  $124 \pm 2$  GPa, respectively, whereas the corresponding values for the intermetallic nanocomposite  $\beta$ -type phase matrix were  $650 \pm 8$  MPa and  $130 \pm 2$  GPa. For each of these properties, the difference in results for the two materials may be attributed to the difference in phase composition and pT.

These findings suggest that the combination of ball-milled of Nb<sub>50</sub>Ti/SWCNTs powder and FAST-SPS may have promise for use in manufacturing load-bearing metallic orthopaedic components, such as the femoral stem of a hip implant and in superconductor magnets (Poloidal Field Coils) in ITER.

The average hardness increased significantly with increasing of SWCNTs wt% at the sintering temperature 1473 K. The increasing average hardness with increasing of SWCNTs wt% at the sintering temperatures of 1473 K at 0.4 to 0.8 wt% of SWCNTs was attributed to the increasing volume fraction of  $\beta$ -type phase together with the embrittlement of  $\beta$ -type phase due to SWCNTs entrapment in the sintered compacts. In other hand SWCNTs increase the ductility and then the fracture toughness by stopping failer of the materials. The superconducting and wear properties will be performed in the near future.

## Acknowledgments

The present work was supported by the Algerian Ministerium of Higher Education and Scientific Research and the PRFU project under contract N° A11N01UN240120220005. These supports are gratefully appreciated.

## Conflicts of Interest

The authors declare no conflict of interest.

## Declaration of Interests

- The authors declare that they have no known competing financial interests or personal relationships that could have appeared to influence the work reported in this paper.

The authors declare the following financial interests/personal relationships which may be considered as potential competing interests.

## References

1. Attar H, Löber L, Funk A, Calin M, Zhang LC, et al. (2015) Mechanical behavior of porous commercially pure Ti and Ti-TiB composite materials manufactured by selective laser melting. *Materials Science and Engineering: A* 625: 350-356.
2. Bönisch M, Stoica M, Calin M (2020) Routes to control diffusive pathways and thermal expansion in Ti-alloys. *Scientific Reports* 10: 1-9. [crossref]
3. Attar H, Calin M, Zhang LC, Scudino S, Eckert J (2014) Manufacture by selective laser melting and mechanical behavior of commercially pure titanium. *Materials Science and Engineering: A* 593: 170-177.
4. Attar H, Prashanth KG, Chaubey AK, Calin M, Zhang LC, et al. (2015) Comparison of wear properties of commercially pure titanium prepared by selective laser melting and casting processes. *Materials Letters* 142: 38-41.
5. Zhang LC, Attar H, Calin M, Eckert J (2016) Review on manufacture by selective laser melting and properties of titanium based materials for biomedical applications. *Materials Technology* 31: 66-76.
6. Lekka CE, Gutiérrez-Moreno JJ, Calin M (2017) Electronic origin and structural instabilities of Ti-based alloys suitable for orthopaedic implants. *Journal of Physics and Chemistry of Solids* 102: 49-61.
7. Bönisch M, Calin M, Van Humbeeck J, Skrotzki W, Eckert J (2015) Factors influencing the elastic moduli, reversible strains and hysteresis loops in martensitic Ti-Nb alloys. *Materials Science and Engineering: C* 48: 511-520. [crossref]
8. Okulov IV, Bönisch M, Okulov AV, Volegov AS, Attar H, et al. (2018) Phase formation, microstructure and deformation behavior of heavily alloyed TiNb- and TiV-based titanium alloys. *Materials Science and Engineering: A* 733: 80-86.
9. Okulov IV, Volegov AS, Attar H, Bönisch M, Ehtemam-Haghighi S, et al. (2017) Composition optimization of low modulus and high-strength TiNb-based alloys for biomedical applications. *Journal of the Mechanical Behavior of Biomedical Materials* 65: 866-871. [crossref]
10. Panigrahi A, Bönisch M, Waitz T, Schafner E, Calin M, et al. (2015) Phase transformations and mechanical properties of biocompatible Ti-Zr16.1 Nb processed by severe plastic deformation. *Journal of Alloys and Compounds* 628: 434-441.
11. Prashanth KG, Zhuravleva K, Okulov I, Calin M, Eckert J, et al. (2016) Mechanical and corrosion behavior of new generation Ti-45Nb porous alloys implant devices. *Technologies* 4: 33.
12. Gennari S, Maglia F, Anselmi-Tamburini U, Spinolo G (2003) SHS (Self-sustained high-temperature synthesis) of intermetallic compounds: effect of process parameters by computer simulation. *Intermetallics* 11: 1355-1359.
13. Liu E, Jia J, Bai Y, Wang W, Gao Y (2014) Study on preparation and mechanical property of nanocrystalline NiAl intermetallic. *Materials & Design* 53: 596-601.
14. Geist D, Gammer C, Rentenberger C, Karnthaler HP (2015) Sessile dislocations by reactions in NiAl severely deformed at room temperature. *Journal of Alloys and Compounds* 621: 371-377. [crossref]
15. Liu E, Gao Y, Bai Y, Yi G, Wang W, et al. (2014) Tribological properties of self-lubricating NiAl/Mo-based composites containing AgVO<sub>3</sub> nanowires. *Materials Characterization* 97: 116-124.
16. Zhang JF, Shen J, Shang Z, Feng ZR, Wang LS, et al. (2012) Microstructure and room temperature fracture toughness of directionally solidified NiAl-Mo eutectic in situ composites. *Intermetallics* 21: 18-25.
17. Zhuravleva K, Bönisch M, Prashanth KG, Hempel U, Helth A, et al. (2013) Production of porous  $\beta$ -Type Ti-40Nb alloy for biomedical applications: Comparison of selective laser melting and hot pressing. *Materials* 6: 5700-5712. [crossref]
18. Bocanegra-Bernal MH, Dominguez-Rios C, Echeberría J, Reyes-Rojas A, Garcia-Reyes A, et al. (2016) Spark plasma sintering of multi-, single/double- and single-walled carbon nanotube-reinforced alumina composites: is it justifiable the effort to reinforce them?. *Ceramics International* 42: 2054-2062.
19. Moshksar MM, Mirzaee M (2004) Formation of NiAl intermetallic by gradual and explosive exothermic reaction mechanism during ball milling. *Intermetallics* 12: 1361-1366.
20. Suryanarayana C (2001) Mechanical alloying and milling. *Progress in Materials Science* 46: 1-184.
21. Beyhaghi M, Kiani-Rashid AR, Kashefi M, Khaki JV, Jonsson S (2015) Effect of powder reactivity on fabrication and properties of NiAl/Al<sub>2</sub>O<sub>3</sub> composite coated on cast iron using spark plasma sintering. *Applied Surface Science* 344: 1-8.
22. Umanskii AP, Polyarus EN, Ukrainets MS, Kapitanchuk LM (2015) Structure and tribotechnical characteristics of NiAl-CrB<sub>2</sub> composite materials and coatings. *Powder Metallurgy and Metal Ceramics* 54: 53-59.
23. Singla D, Amulya K, Murtaza Q (2015) CNT reinforced aluminium matrix composite-a review. *Materials Today: Proceedings* 2: 2886-2895.
24. Alizadeh A, Abdollahi A, Biukani H (2015) Creep behavior and wear resistance of Al 5083 based hybrid composites reinforced with carbon nanotubes (CNTs) and boron carbide (B<sub>4</sub>C) *Journal of Alloys and Compounds* 650: 783-793.
25. Zhang M, Hou X, Wang J, Li M, Hu S, et al. (2014) Interwoven Si@C/CNTs&CNFs composites as anode materials for Li-ion batteries. *Journal of Alloys and Compounds* 588: 206-211.
26. Peng T, Chang I (2014) Mechanical alloying of multi-walled carbon nanotubes reinforced aluminum composite powder. *Powder Technology* 266: 7-15.

27. Vishlaghi MB, Ataia A (2014) Investigation on solid solubility and physical properties of Cu-Fe/CNT nano-composite prepared via mechanical alloying route. *Powder Technology* 268: 102-109.
28. Mazaheri M, Mari D, Hesabi ZR, Schaller R, Fantozzi G (2011) Multi-walled carbon nanotube/nanostructured zirconia composites: outstanding mechanical properties in a wide range of temperature. *Composites Science and Technology* 71: 939-945.
29. Pang LX, Sun KN, Ren S, Sun C, Fan RH, et al. (2007) Fabrication and microstructure of Fe3Al matrix composite reinforced by carbon nanotube. *Materials Science and Engineering: A* 447: 146-149.
30. Schmidt R, Pilz S, Lindemann I, Damm C, Hufenbach J, et al. (2017) Powder metallurgical processing of low modulus  $\beta$ -type Ti-45Nb to bulk and macro-porous compacts. *Powder Technology* 322: 393-401.
31. Wang Q, Cui G, Chen H (2021) Effect of the Ta addition on densification and mechanical properties of NbTi alloys prepared by SPS. *Journal of Alloys and Compounds* 868: 159106.
32. Helth A, Gostin PF, Oswald S, Wendrock H, Wolff U, et al. (2014) Chemical nanoroughening of Ti40Nb surfaces and its effect on human mesenchymal stromal cell response. *Journal of Biomedical Materials Research Part B: Applied Biomaterials* 102: 31-41. [[crossref](#)]
33. Gostin PF, Helth A, Voss A, Suetpitz R, Calin M, et al. (2013) Surface treatment, corrosion behavior, and apatite-forming ability of Ti-45Nb implant alloy. *Journal of Biomedical Materials Research Part B: Applied Biomaterials* 101: 269-278. [[crossref](#)]
34. Zhuravleva K, Bönisch M, Scudino S, Calin M, Schultz L, et al. (2014) Phase transformations in ball-milled Ti-40Nb and Ti-45Nb powders upon quenching from the  $\beta$ -phase region. *Powder Technology* 253: 166-171.
35. Kauschke V, Gebert A, Calin M, Eckert J, Scheich S, et al. (2018) Effects of new beta-type Ti-40Nb implant materials, brain-derived neurotrophic factor, acetylcholine and nicotine on human mesenchymal stem cells of osteoporotic and non-osteoporotic donors. *PLoS One* 13: e0193468. [[crossref](#)].
36. Attar H, Calin M, Zhang LC, Scudino S, Eckert J (2014) Manufacture by selective laser melting and mechanical behavior of commercially pure titanium. *Materials Science and Engineering: A* 593: 170-177.
37. Helth A, Pilz S, Kirsten T, Giebeler L, Freudenberger J, et al. (2017) Effect of thermomechanical processing on the mechanical biofunctionality of a low modulus Ti-40Nb alloy. *Journal of the Mechanical Behavior of Biomedical Materials* 65: 137-150. [[crossref](#)]
38. Schmidt R, Hoffmann V, Helth A, Gostin PF, Calin M, et al. (2016) Electrochemical deposition of hydroxyapatite on beta-Ti-40Nb. *Surface and Coatings Technology* 294: 186-193.
39. Gostin PF, Helth A, Voss A, Suetpitz R, Calin M, et al. (2013) Surface treatment, corrosion behavior, and apatite-forming ability of Ti-45Nb implant alloy. *Journal of Biomedical Materials Research Part B: Applied Biomaterials* 101: 269-278. [[crossref](#)]
40. Zhuravleva K, Chivu A, Teresiak A, Scudino S, Calin M, et al. (2013) Porous low modulus Ti40Nb compacts with electrodeposited hydroxyapatite coating for biomedical applications. *Materials Science and Engineering: C* 33: 2280-2287.
41. Abdi S, Oswald S, Gostin PF, Helth A, Sort J, et al. (2016) Designing new biocompatible glass-forming Ti75-xZr10NbxSi15 (x=0, 15) alloys: corrosion, passivity, and apatite formation. *Journal of Biomedical Materials Research Part B: Applied Biomaterials* 104: 27-38.
42. Hynowska A, Blanquer A, Pellicer E, Fornell J, Surinach S, et al. (2015) Nanostructured Ti-Zr-Pd-Si-(Nb) bulk metallic composites: Novel biocompatible materials with superior mechanical strength and elastic recovery. *Journal of Biomedical Materials Research Part B: Applied Biomaterials* 103: 1569-1579.
43. Calin M, Helth A, Gutierrez Moreno JJ, Boenisch M, Brackmann V, et al. (2014) Elastic softening of  $\beta$ -type Ti-Nb alloys by indium (In) additions. *Journal of the Mechanical Behavior of Biomedical Materials* 39: 162-174. [[crossref](#)]
44. Hynowska A, Pellicer E, Fornell J, Gonzalez S, van Steenberghe N, et al. (2012) Nanostructured  $\beta$ -phase Ti-31.0 Fe-9.0 Sn and sub- $\mu$ m structured Ti-39.3 Nb-13.3 Zr-10.7 Ta alloys for biomedical applications: Microstructure benefits on the mechanical and corrosion performances. *Materials Science and Engineering: C* 32: 2418-2425.
45. Calin M, Gebert A, Ghinea AC, Gostin PF, Abdi S, et al. (2013) Designing biocompatible Ti-based metallic glasses for implant applications. *Materials Science and Engineering: C* 33: 875-883.
46. Gutierrez Moreno JJ, Boenisch M, Panagiotopoulos NT, Calin M, Papageorgiou DG, et al. (2017) Ab-initio and experimental study of phase stability of Ti-Nb alloys. *Journal of Alloys and Compounds* 696: 481-489.
47. Bendjemil B, Borowiak-Palen E, Graff A, Pichler T, Knupfer M, et al. (2004) Elimination of metal catalyst and carbon-like impurities from single-wall carbon nanotube raw material. *Applied Physics A* 78: 311-314.
48. Selbmann D, Bendjemil B, Leonhardt A, Pichler T, Täschner C, et al. (2008) A parametric study of the synthesis and purification of single-walled carbon nanotubes using the high-pressure carbon monoxide process. *Applied Physics A* 90: 637-643.
49. Bendjemil B, Mouyane M, Noudem JG, Bernard J, Reboul JM, et al. (2018) Sintering Behavior and Properties of cBN/TiC/SWCNTs or NC Ceramics Matrix Nanocomposites (CMNC's) by Field Activated Spark Plasma Sinter.
50. Bendjemil B, Noudem JG, Mouyane M, Bernard J, Guhel Y, et al. (2020) Study of the Nanocomposite Mo2C (1-x)-TiC (x)-SWCNTs by Field Activated Spark Plasma Sintering Process. *Journal of Advances in Nanotechnology* 1: 30-47.
51. Le Bail A (1995) Modelling the silica glass structure by the Rietveld method. *Journal of Non-Crystalline Solids* 183: 39-42.
52. Moffat DL, Kattner UR (1988) The stable and metastable Ti-Nb phase diagrams. *Metallurgical Transactions A* 19: 2389-2397.
53. Zhuravleva K, Bönisch M, Scudino S, Calin M, Schultz L, et al. (2014) Phase transformations in ball-milled Ti-40Nb and Ti-45Nb powders upon quenching from the  $\beta$ -phase region. *Powder Technology* 253: 166-171.
54. Zhuravleva K, Scudino S, Khoshkhou MS, Gebert A, Calin M, et al. (2013) Mechanical Alloying of  $\beta$ -Type Ti-Nb for Biomedical Applications. *Advanced Engineering Materials* 15: 262-268.
55. Zhang DZ, Qin ML, Zhang L, Qu XH (2012) Fabrication and characterization of nanocrystalline Nb-W-Mo-Zr alloy powder by ball milling. *International Journal of Refractory Metals and Hard Materials* 32: 45-50.
56. Hempel U, Müller K, Preissler C, Noack C, Boxberger S, et al. (2016) Human bone marrow stromal cells: a reliable, challenging tool for in vitro osteogenesis and bone tissue engineering approaches. *Stem Cells International* 14. [[crossref](#)]
57. Herzer R, Gebert A, Hempel U, Hebenstreit F, Oswald S, et al. (2021) Rolled-Up Metal Oxide Microscaffolds to Study Early Bone Formation at Single Cell Resolution. *Small* 17: 2005527. [[crossref](#)]
58. Vishnu J, Calin M, Pilz S, Gebert A, Kaczmarek B, et al. (2020) Superhydrophilic nanostructured surfaces of beta Ti29Nb alloy for cardiovascular stent applications. *Surface and Coatings Technology* 396: 125965.
59. Charifoulline Z (2006) Residual resistivity ratio (RRR) measurements of LHC superconducting NbTi cable strands. *IEEE Transactions on Applied Superconductivity* 16: 1188-1191.
60. Fang L, Feng L, Huixian G, Chao C, Bo L, et al. (2015) Comparison and analysis of twist pitch length test methods for ITER Nb3Sn and NbTi strands. *Rare Metal Materials and Engineering* 44: 2095-2099.
61. Dresselhaus MS, Dresselhaus G, Avouris P (2001) Carbon Nanotubes Synthesis, Structure, Properties, and Applications.
62. Ugawa A, Rinzler AG, Tanner DB (1999) Far-infrared gaps in single-wall carbon nanotubes. *Physical Review B* 60: R11305.
63. Hilt O, Brom HB, Ahlskog M (2000) Localized and delocalized charge transport in single-wall carbon-nanotube mats. *Physical Review B* 61: R5129.
64. Ahn JS, Kim KH, Noh TW, Riu DH, Boo KH, et al. (1995) Effective-medium theories for spheroidal particles randomly oriented on a plane: Application to the optical properties of a SiC whisker-Al2O3 composite. *Physical Review B* 52: 15244. [[crossref](#)]

#### Citation:

Bendjemil B, Safi K, Kouahla I, Guillome Noudem J, Mouyane M, et al. (2022) Manufacturing of  $\beta$ -type NbXTi ( $X=50$  at%)/SWCNTs Matrix Nanocomposites by FAST-SPS: For Metallic Orthopedic Components and Superconductor Magnets in ITER. *Nanotechnol Adv Mater Sci* Volume 5(2): 1-18.